

On the sensitivity of extrasolar mass–loss rate ranges: HD 209458b a case study

C. Villarreal D’Angelo¹, M. Schneider^{1,2}, A. Costa^{1,2}, P. Velázquez³, A. Raga³, A. Esquivel³

¹*Instituto de Astronomía Teórica y Experimental, IATE (CONICET and Universidad Nacional de Córdoba), Córdoba, Argentina*

²*Faculty of Ciencias Exactas, Físicas y Naturales Universidad Nacional de Córdoba, Argentina*

³*Instituto de Ciencias Nucleares, Universidad Nacional Autónoma de México, DF, Mexico*

Accepted 2013 November 28. Received 2013 November 12; in original form 2013 April 2013

ABSTRACT

We present a 3D hydrodynamic study of the effects that different stellar wind conditions and planetary wind structures have on the calculated Ly α absorptions produced by a cometary tail during transit. We concentrate, as a case study, on the known HD 209458b case.

Initially, we assume a broad range of possible planetary mass-loss rate values: $\dot{M}_p = [1 - 7] \times 10^{10} \text{ g s}^{-1}$. Then, by comparing the observational Ly α absorption with the numerically derived ones, we could constrain the \dot{M}_p values within the given range. We find that the planetary mass-loss rate does not change dramatically for large changes in stellar wind speeds $\sim [250 - 800] \text{ km s}^{-1}$ and temperature $\sim [3 - 7] \times 10^6 \text{ K}$ while keeping fixed the stellar mass-loss rate ($\dot{M}_\star = 9.0 \times 10^{-14} M_\odot \text{ yr}^{-1}$). The \dot{M}_p range found is $\sim [3 - 5] \times 10^{10} \text{ g s}^{-1}$, depending upon the efficiency of the stellar wind to transport heat (polytropic index $\Gamma \sim [1.01 - 1.13]$), leading to different stellar wind speeds. Several models with anisotropic evaporation profiles for the planetary escaping atmosphere were carried out, showing that both, the escape through polar regions, resembling the emission associated with reconnection processes, and through the night side, produced by a strong stellar wind that compresses the planetary atmosphere and inhibits its escape from the day hemisphere yields larger absorptions than an isotropic planetary wind.

Key words: hydrodynamics - planetary systems.

1 INTRODUCTION

The giant hot Jupiter HD 209458b was the first extrasolar planet observed in transit (Charbonneau et al. 2000; Henry et al. 2000) and the first for which far-ultraviolet space observations were obtained with the *Hubble Space Telescope*/Space Telescope Imaging Spectrograph (STIS) instrument.

An initial analysis of this data set was performed by Vidal-Madjar et al. (2003, hereafter VM03). These authors carried out observations in the Ly α line (at 1215.67 Å), measuring an extra mid-transit absorption (relative to the level of the continuum) of 15 ± 4 per cent over a range of $[-130, 200] \text{ km s}^{-1}$. Also, the spectral absorption during transit was deeper on the blue side of the stellar line. These results lead the authors to claim the existence of an extended exosphere (as predicted in Schneider et al. 1998). Later, a new analysis of the same data set was performed by Ben-Jaffel (2007, 2008, hereafter BJ07 and BJ08, respectively) to account for the effect of stellar variability on the transit depths. In these works, the authors measured an absorption of 8.9 ± 2.1 per cent in the $\pm 200 \text{ km s}^{-1}$ velocity range, which they explained as the effective absorption made by a cloud of $\sim 2.7R_p$ (which is smaller than the planetary Roche lobe), implying no direct evidence for a

cometary tail in the data.

These differences in the measurement of the Ly α absorption led to a discussion in the literature (see BJ07; BJ08; Vidal-Madjar et al. 2008). BJ07 developed a new correction for the geocoronal contamination that led him to redefine the wavelength limits used for calculating the transit depth. Unlike BJ07, in Vidal-Madjar et al. (2008, hereafter VM08) the authors argued that the discrepancies were mainly due to the use of different wavelength (or velocity) ranges to convert the spectra, as a function of time, into a single absorption depth, and to the reference flux used to correct the intrinsic stellar flux variation. Hence, they claimed that larger wavelength domains imply a diluted absorption signal with a consequently lower absorption depth. Koskinen et al. (2010) argued that the apparent disagreement between BJ07 and VM03 arises not only from different definitions of the transit depth but also from differences in the treatment of the data. However, they agreed with VM08 that, as the core of the absorption line is optically thick up to the Roche lobe, the atmosphere must be evaporating.

Another issue related to the transit absorption of Ly α photons in the velocity range of $[-130, 100] \text{ km s}^{-1}$, is the origin of the high-velocity neutral gas. To answer this question, and arguing that the stellar radiation pressure is not enough to explain the observations,

Holmström et al. (2008) proposed that the high-velocity neutral hydrogen can be produced by charge exchange between the neutral atmosphere and the stellar wind ions. The stellar wind velocity they used was somehow low (50 km s^{-1}) in comparison to the typical solar wind conditions. Following this idea, and employing a more typical stellar wind velocity (450 km s^{-1}), Ekenbäck et al. (2010) modelled the production of neutral hydrogen and matched the signature of the Ly α absorption profile.

Also, other atmosphere mass-loss models due to EUV input from host stars can also account for the Ly α absorption and the high-velocity neutral gas (see VM03; Lecavelier des Etangs et al. 2004; Yelle 2004; Tian et al. 2005; García Muñoz 2007; Schneider et al. 2007; Murray-Clay et al. 2009; Koskinen et al. 2010; Guo 2011). The proximity of the planet to its parent star ($\approx 0.045 \text{ au}$) and the consequent non-thermal heating of the upper planetary atmosphere (up to 10^4 K) by stellar X-ray and EUV photons, would produce a hydrodynamic blow-off of the upper atmospheric layers. Lecavelier des Etangs et al. (2004) showed that this mechanism may be enhanced by tidal forces that could pull the exobase level up to the Roche limit, and predicted an asymmetric shape for the transit curve due to the comet-like tail produced by the evaporating atmosphere of the planet. This scenario was reinforced by the detection of hydrodynamic escape signals in C II and O I lines (VM08), Na I D lines (Vidal-Madjar et al. 2011) and Si III line (Linsky et al. 2010). Though, according to Ehrenreich et al. (2008) the observations are not yet sufficient to establish the presence of a tail.

The question whether the STIS observations are correctly explained as a planetary wind driven by photoionization or by charge exchange (or both processes) remains open. The works of Ben-Jaffel & Sona Hosseini (2010) and Guo (2011) showed that either energetic neutral HI of stellar origin or thermal HI populations in the planetary atmosphere could fit the Ly α observations. Koskinen et al. (2010) introduced a generic method to analyse and interpret ultraviolet transit light curves. They applied it to the measurements of HD 209458b, and showed that the observations can be explained by absorption in the upper atmosphere without the need of ENAs.

Almost all models that try to explain the observed Ly α absorption of HD209458b produce mass-loss rates that are several times 10^{10} g s^{-1} . For example, Yelle (2004, see correction in Yelle 2006), find $\dot{M}_p = 4.7 \times 10^{10} \text{ g s}^{-1}$, Tian et al. (2005) find $\dot{M}_p < 6 \times 10^{10} \text{ g s}^{-1}$, García Muñoz (2007) finds $\dot{M}_p = 6.1 \times 10^{10} \text{ g s}^{-1}$, Guo (2011) finds $\dot{M}_p = 3.4 \times 10^{10} \text{ g s}^{-1}$, and Murray-Clay et al. (2009) find $\dot{M}_p \sim 2 \times 10^{10} \text{ g s}^{-1}$.

We need to keep in mind that the presence of a planetary magnetic field can lead to significant changes in the upper atmosphere of planets and consequently can lower the planetary mass-loss rate. Adams (2011), considering an outflow modulated by a magnetic field, estimated a planetary outflow of the order of $\sim 10^9 \text{ g s}^{-1}$ produced mainly in the polar regions.

In Schneider et al. 2007 (2007, hereafter SCH07) a model for the cometary exosphere around HD 209458b was presented via the assumption that it is dynamically similar to the ion tail of a comet (see e.g. Rauer et al. 1997). 3D hydrodynamic simulations of the interaction between the material, which is being photoevaporated from the planetary atmosphere, and the impinging stellar wind lead to the conclusion that a cometary structure, obtained as a consequence of the simulated wind interaction, must have a size that grows for increasing values of the planetary mass-loss rate \dot{M}_p , and therefore produces a Ly α absorption of the stellar emission which is a monotonically increasing function of \dot{M}_p . In

this model, a fixed solar-like value for the stellar wind speed and an isotropic emission were assumed. From the comparison with the observations of VM03 for the Ly α absorption, the authors estimated the mass-loss rate as $\dot{M}_p \sim 10^{10} \text{ g s}^{-1}$.

In this work, despite the mentioned discussions in literature (not yet settled), and assuming the existence of an evaporating atmosphere, we study the influence of different stellar wind temperatures and velocities, on the planetary mass-loss rate. In spite of the oversimplifications of our model a variation of the stellar wind speed and temperature, in a reasonable range, gives different values of \dot{M}_p . Thus, different combinations of (v_0, \dot{M}_p) (v_0 is the stellar wind speed at the planet position) could give account of the absorption derived from the observations. We explore the allowed range of this combination of parameters and discuss its implication on the determined stellar-planetary parameters. The procedure consists of assuming values of \dot{M}_p within a range of possible ones. Then, to constrain the planetary mass-loss rate the numerically derived Ly α absorption is compared with the observations.

The first part of the study is performed assuming an isotropic planetary wind for a thermalized atmosphere. In the second part, we explore the effect of different structures of planetary wind emissions resembling different cases such as the day/night asymmetry due to a tidally locked planetary motion, and polar winds due to emission associated with reconnection processes (see Fig. 1). We emphasize that this final part only presents toy atmospheric models which illustrate how more detailed escaping atmosphere models could modify the predicted Ly α absorption.

We describe our numerical approach in §2, the anisotropic planetary ejection wind models in §3, and discuss the consequences of the results in §4. Finally, we summarize the results and conclusions in §5.

2 THE METHOD

The simulation: The 3D hydrodynamic simulations were carried out with the Yguazú code (Raga, Navarro-González & Villagrán-Muniz 2000) as described in SCH07 that evolves the ideal HD equations given, in conservative form, by

$$\frac{\partial \rho}{\partial t} + \nabla \cdot (\rho \mathbf{u}) = 0 \quad (1)$$

$$\frac{\partial \rho \mathbf{u}}{\partial t} + \nabla \cdot (\rho \mathbf{u} \mathbf{u} + p \mathbf{I}) = \rho \mathbf{g} \quad (2)$$

and

$$\frac{\partial \varepsilon}{\partial t} + \nabla \cdot (\mathbf{u}(\varepsilon + p)) = \rho \mathbf{g} \cdot \mathbf{u}, \quad (3)$$

where ρ indicates the density; \mathbf{u} the velocity; \mathbf{g} is the gravity, p is the pressure and ε is the total energy density given by

$$\varepsilon = \frac{p}{\gamma - 1} + \frac{1}{2} \rho u^2, \quad (4)$$

where γ is the ratio of specific heats. For the simulations we adopt $\gamma = \Gamma$ with Γ being the polytropic index.

A six level, binary adaptive grid with a maximum resolution of $1.8 \times 10^4 \text{ km}$ was used. A computational domain of $7.4 \times 10^7 \text{ km}$ (or 0.49 au), 1.85×10^7 and $7.4 \times 10^7 \text{ km}$ (in the x -, y - and z -directions, respectively) was employed. The coordinate system is such that the star is placed at the centre of the domain and the planet is orbiting in the xz -plane. We define two inner boundaries, one

Γ	T_0 MK	T_w MK	v_w (km s ⁻¹)
1.01	3	2.8	372
	4	3.8	488
	5	4.7	594
	6	5.7	692
	7	6.7	784
1.13	3	1.3	205
	4	2.0	349
	5	2.6	475
	6	3.2	590

Table 1. Determination of the stellar wind inner boundary parameters.

that belongs to the planet, whose location is updated at each time step according to the orbital motion, forced to have the maximum resolution, and the other is located at a fixed radius from the center of the computational domain, where the stellar wind is imposed continuously.

The gravity of both, planet and star were included in the simulations. The radiation pressure was considered by reducing the effective gravity as in VM03, i.e. the Ly α radiation pressure is assumed to be 0.7 times the stellar gravity.

The stellar wind: The G0 V star (HD 209458) of $1.148M_\odot$ was simulated to have a non magnetized isotropic wind, with mass-loss rate of $\dot{M}_* = 9.0 \times 10^{-14} M_\odot \text{ yr}^{-1}$ (corresponding to an ion flux of $5.2 \times 10^{36} \text{ s}^{-1}$) fixed for all the models. The stellar inner boundary, where the wind is imposed continuously, is launched at $R = 6.9R_*$. For all the models used, this position is located beyond the critical point where the wind velocity is still increasing, before the terminal speed is reached. We used several polytropic models to calculate reasonable initial conditions of the almost thermally driven wind (with values of the polytropic index close to 1). In this way, we could vary the velocity in the range $\sim [200 - 800] \text{ km s}^{-1}$, at the radius where the stellar wind is imposed. These results are in agreement with the wind velocity profiles in Vidotto et al. (2012) and shown in Table 1. In the table, T_0 , is the coronal temperature, T_w and v_w are, respectively, the temperature and velocity at the position where the wind is launched, calculated using two polytropic wind models (with Γ being the polytropic index $\Gamma = [0.01 - 1.13]$). The density varies consistently with the fixed value of $\dot{M}_* = 4\pi\rho v R_*^2$ ($R_* = 7.97 \times 10^5 \text{ km}$ being the stellar radius). At the position of the planet the density values ($[1.2 - 4.1] \times 10^{-20} \text{ gr cm}^{-3}$) are consistent with the values found by other authors (e.g. Vidotto et al. 2012, Llama et al. 2011).

The planet: It was initially modelled to have an isotropic evaporating wind, emitted from $3R_p$ with a velocity $v_p = 10 \text{ km s}^{-1}$ (where $R_p = 1.4R_{Jup}$ and $M_p = 0.69M_{Jup}$). The boundary condition for the base plasma temperature was fixed at $T_0 = 10^4 \text{ K}$ and we varied the mass-loss rate between $[1-7] \times 10^{10} \text{ g sec}^{-1}$ corresponding to number densities between $[9.4 \times 10^6 - 6.6 \times 10^7] \text{ cm}^{-3}$ at the base of the inner boundary. It is important to emphasize that we do not solve the problem of the production of a wind from the irradiated surface of the planet (for works that handle the wind production see; e.g. Preusse et al. (2005) and Tian et al. (2005)). Instead, we assume that the planet ejects an (initially) isotropic wind from its upper atmosphere with parameters that are consistent with the works of Tian et al. (2005), Koskinen et al. (2010), Murray-Clay et al. (2009) and Guo (2011). The density profile inside the inner boundary ($r < 3R_p$) is slightly different to the one proposed in Tian et al. (2005), since it has a slower increase towards the surface of the planet. This does not affect the calculated

absorption, since the material within the Roche lobe ($< \sim 3R_p$) absorbs in the range cover by the Ly α geocoronal contamination. Assuming an escaping planetary wind is a way of eliminating from our simulations the complex problem of the calculation of the photoevaporation of the planetary atmosphere.

In addition four models with an anisotropic planetary wind were run, where the emitting surface was changed, and the wind velocities were modified such that the mass-loss rates were conserved. These models are thoroughly explained in Section §3.

Computation of the Ly α absorption: From the computed density, velocity and temperature structures we calculated the Ly α absorption associated with a planetary transit of the stellar disc. The computational grid is oriented at an angle $i = 86^\circ.67$, i.e. the angle between the orbital axis and the line of sight of HD 209458b. The optical depth is obtained as

$$\tau_\nu = \int n_{HI} \sigma_0 \phi(\Delta\nu) ds, \quad (5)$$

for all lines of sight, where the integral goes from the surface of the star to the edge of the computational domain, n_{HI} is the neutral hydrogen number density, ν is the frequency and $\Delta\nu = \nu - \nu_0$ is the offset from the line centre, $\sigma_0 = 0.01105 \text{ cm}^2$ (Osterbrock 1989) is the Ly α absorption cross-section at the line centre, and s is the length measured along the line of sight. $\phi(\Delta\nu)$ is the Doppler line profile given by

$$\phi(\Delta\nu) = \left(\frac{m_H}{2\pi kT} \right)^{1/2} e^{-m_H \Delta\nu^2 / 2kT} \frac{c}{\nu_0}, \quad (6)$$

where m_H is the proton mass, c is the velocity of light, k is the Boltzmann constant, T is the gas temperature, $\Delta u = u_r - u_F$, u_F is the flow velocity along the line of sight, and $u_r = c\Delta\nu/\nu_0$ is the radial velocity associated with a frequency shift $\Delta\nu$ from the line centre ν_0 .

The stellar wind is assumed to be a fully ionized H gas so it does not contribute to the absorption (i. e., $n_{HI} = 0$ for equation 5). Also, the planetary wind is supposed to be fully neutral [so that $n_{HI} = \rho/(1.3m_H)$, where ρ is the gas density]. With the interaction the planetary material is heated and mixed with the ionized stellar wind. We consider that the planetary material temperature above its ionization value ($T \sim 10^5 \text{ K}$) will not contribute to the absorption. The material from the planetary wind is identified with an advected passive scalar in the simulations.

We consider that at a given frequency the stellar disc emits a uniform specific intensity $I_{\nu,*}$ (i.e., we neglect the centre-to-limb variation). We then compute the intensity seen by the observer ($I_\nu = I_{\nu,*} e^{-\tau_\nu}$, with τ_ν given by equation 5). Finally, we carry out an integration of the intensity over the stellar disc (for which we assume an $R_* = 1.12R_\odot$ photospheric radius) in order to simulate an observation in which the stellar disc is unresolved.

The total intensity decrease due to the absorption resulting from the presence of the planetary exosphere was computed as a frequency average to obtain

$$I/I_* = \frac{1}{\nu_2 - \nu_1} \int_{\nu_1}^{\nu_2} \langle e^{-\tau_\nu} \rangle d\nu, \quad (7)$$

where $\langle e^{-\tau_\nu} \rangle$ is the absorption averaged over the stellar disc, and ν_1 and ν_2 correspond to the limits of the velocity range.

Choice of the absorption range: The averaging of the absorption over frequency was done, taking the ratio between the emission (as a function of frequency) observed during transit and the ‘stellar emission’ (i. e., the emission observed away from transit), and then integrating within a frequency band which includes the Ly α line

(for a more complete description see SCH07). Hence, the values of the absorptions depend strongly on the integration range utilized, and since several authors have found different absorption values, due to the choice in wavelength ranges that were employed, it is important to take them into account when analysing the results.

For instance, VM03 reported an ~ 15 per cent Ly α absorption integrating in the range $[-130, 100]$ km s $^{-1}$, BJ07 reported a ~ 8.9 per cent absorption in the range $[-200, 200]$ km s $^{-1}$ and Vidal-Madjar et al. (2004, hereafter VM04) an ~ 5 per cent Ly α absorption in the range $[-320, 200]$ km s $^{-1}$.

With the purpose of comparing with the observations (VM03; VM04; BJ07), to perform the Ly α integration we swept the three mentioned velocity ranges, as shown in columns 4–6 in Table 2. The $[-130, 100]$ km s $^{-1}$ was simulated to have $[-120, 100]$ km s $^{-1}$ in all models (this is due to the discrete jumps in velocity, every 20 km s $^{-1}$, when calculating the absorption). For all cases we took into account the geocoronal contamination, performing the correction suggested in VM03, and excluding the central part of the line, from 1215.5 to 1215.8 Å (i.e., $[-40, 40]$ km s $^{-1}$). To identify the absorption ranges we adopt the convention used in VM08: line core interval (C: [19-11] per cent) measured by VM03, intermediate line range (I: [11-6.8] per cent) measured by BJ07 and whole line range (W: [7-3] per cent) measured by VM04.

3 ANISOTROPIC PLANETARY WIND MODELS

The rotational periods of ‘hot Jupiters’ are likely synchronized with their orbital periods, hence only one side of the planet is irradiated. For this reason, it is not a bad idea to relax the assumption of isotropic, and try to see how different structures of planetary winds affect the measured absorptions. Also, going a little further in this line of thought, and based on the discussion in Adams (2011) where the probable existent planetary magnetic field is simulated, we propose a scenario where the escaping material occurs in the polar regions. With this in mind we present four oversimplified alternative inner boundaries for the planet, that we named as follows

- *Day*: escape only through the illuminated hemisphere. This is the case when the energy deposited in the day side cannot be re-distributed to the night side, as would happen when the horizontal advection time is longer than the radial advection time (see discussion in Murray-Clay et al. 2009).
- *Day-Night*: 75 per cent of the mass escapes from the day side and 25 % from the night side. This happens because some of the energy deposited on the illuminated hemisphere is transported to the other hemisphere, but a variation remains (Yelle 2004).
- *Night*: escape only through the night side. A strong stellar wind may compress the atmosphere and inhibit its escape from the day hemisphere (García Muñoz 2007).
- *Polar*: escape through the poles resembling reconnection processes of a dipolar planetary magnetic field with the magnetic field carried out by the stellar wind (Adams 2011). In our model the wind is emitted from the polar surfaces with areas determined by the solid angle $2\pi(1 - \cos(\theta))$ sr, where θ is measured from the z axis and has a value of $\pi/4$.

To simulate all the anisotropic models we chose the stellar parameters of one isotropic model corresponding to the coronal temperature $T_0 = \text{MK}$ and polytropic index $\Gamma = 1.13$. For the planet, the wind velocity is such that the mass-loss rate is the same for all models ($\dot{M}_p = 3 \times 10^{10}$ g s $^{-1}$), i.e. $V_p = 2V_{p(\text{isotropic})}$ for the Day and Night models, since the surface from which the wind is

emitted is halved. For the Day-Night the velocity is distributed according to the mass-loss rate, i.e. $V_p(\text{Day}) = 1.5V_{p(\text{isotropic})}$, and $V_p(\text{Night}) = 0.5V_{p(\text{isotropic})}$. Finally, the velocity distribution for the Polar model is $V_p(\text{Polar}) = 3.4V_{p(\text{isotropic})}$. The absorption was calculated in the same way as the isotropic wind model. Fig. 1 displays a scheme of the ‘planetary wind’ for each ‘anisotropic model’.

4 RESULTS & DISCUSSION

4.1 Isotropic planetary wind models

In SCH07, typical solar wind conditions were employed to simulate the interaction with the escaping planetary atmosphere, and to compute the resulting absorption. The ~ 500 km s $^{-1}$ stellar wind velocity used in SCH07 led to an $\dot{M}_p \sim 1.1 \pm 0.2 \times 10^{10}$ g s $^{-1}$ estimate (obtained by adjusting the computed absorption to the value of the absorption reported by VM04).

One of the aims of this work is to explore the effect of several wind speeds v_o , at the orbital position and coronal temperatures T_o on the inferred \dot{M}_p . For each model, columns 1-3 of Table 2 show the values of T_o , v_o and \dot{M}_p , respectively. The table, also displays the maximum transit absorption depths for each model calculated for the spectral domains as defined by VM04, BJ07 and VM03 (columns 4 to 6, C, I and W, respectively) and the transit time (Δt)¹. The results are divided in two parts, the upper part, that corresponds to models with the initial conditions obtained with $\Gamma = 1.01$, and the lower one, that corresponds to models with $\Gamma = 1.13$. Columns 4-6 show the maximum absorption values when excluding the part of the spectrum contaminated by the geocoronal Ly α emission. Note that the calculated absorptions correspond only to the contribution of the tail; the material close to the atmosphere has a radial speed of ~ 10 km s $^{-1}$ which falls within the subtracted speed range.

When comparing among the models some general trends can be noted. Larger absorption values are obtained when lowering the coronal temperature, and/or the stellar wind velocity, or by increasing the planetary mass-loss rate. This last trend is easily explained since as more planetary material is ejected a larger column density is obtained, and consequently a larger absorption can be expected. Higher coronal temperatures produce an increase of the temperature gradient - between the stellar wind and the neutral planetary atmosphere ($\sim 10^4$ K) - causing a larger heat transfer which increases the ionization rate, thus lowering the absorption. Also, higher stellar wind speeds (due to higher T_0 or lower Γ values) result in a consequent larger stellar ram pressures that hinders the expansion of the planetary wind, reducing the absorption and transit time.

The dependence of the transit time on T_0 and v_o obeys the same mechanisms as the absorption. That is, as an increase in T_0 is accompanied by an increase in both, the ionization rate and the stellar ram pressure, it produces changes in the size and structure of the escaping material. More specifically, a larger ram pressure produces a more radially aligned wake, and a more effective ionization leads to a smaller size of the absorbing tail, and hence to shorter transit times.

For $\Gamma = 1.13$ and all T_0 the models with $\dot{M}_p = 3 \times 10^{10}$ g s $^{-1}$ (highlighted values in the lower panel of Table 2) are the ones that better adjust the observational values for the three spectral domains, i.e., they fit the limits given by VM03 ([19-11] per cent), BJ07 ([11-6.8] per cent) and VM04 ([7-3] per cent). Whereas, for the models with $\Gamma = 1.01$ larger \dot{M}_p are required (highlighted in

¹ We refer to the transit time as the interval while there is Ly α absorption

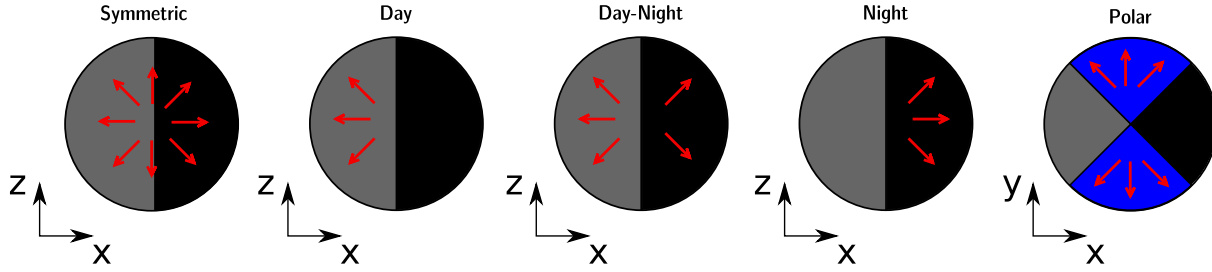


Figure 1. Schemes of inner boundary setups for the different planetary wind models corresponding to isotropic emission (first panel), only day emission (second panel), day/night asymmetry (third panel), only night emission (fourth panel) and polar emission (fifth panel).

the upper panel of Table 2). $\Gamma = 1.01$ implies a more efficient heat transfer, hence the resulting stellar wind velocity and temperature at the orbital position will be larger than for $\Gamma = 1.13$ resulting in lower absorption values.

Figs 2(a)-(c) display a comparison of the global density distribution observed on the orbital plane for models with the same $\dot{M}_p = 3 \times 10^{10} \text{ g s}^{-1}$, noted in last column of Table 2 as a, b and c, respectively. Figs 2(a) and (b) have the same coronal temperature (3 MK) and different v_o (or Γ) (429 km s $^{-1}$ and 247 km s $^{-1}$, respectively), while Figs 2(b) and (c) have the same Γ and different temperatures (3 and 6 MK, respectively). The arrow in Fig. 2(a) indicates the line-of-sight direction. Fig. 2(a) shows a slightly more radially collimated tail than the ones in Fig. 2(b) due to higher v_o . When comparing Figs 2(b) and (c) we see again that the comet-like tail for the larger T_0 model becomes more oriented along the radial direction, as noted earlier. To resume, higher stellar wind speeds relative to the orbital one ($v_{orb} \approx 146 \text{ km s}^{-1}$) imply straighter tails.

Figs 3(a)-(c) show the density distribution of the absorbing material on the orbital plane and for the same cases as those in Figs 2(a)-(c), revealing some small changes of the absorbing areas in line with the discussion given above.

By comparing the isotropic models with the observations it is possible to estimate \dot{M}_p that match the proposed observational absorption ranges for a given T_0 and v_o pair. Relatively low coronal temperature values ($T_0 \approx 3 \text{ MK}$) together with a range of $v_o \sim (250 - 430) \text{ km s}^{-1}$ values (e.g. models a and b of Table 2) are associated with $\dot{M}_p \approx 3 \times 10^{10} \text{ g s}^{-1}$ independently of the heat transport efficiency ($\Gamma \sim [1.01 - 1.13]$). Intermediate and high values of the coronal temperatures ($T_0 \approx (4 - 7) \text{ MK}$) together with a broad range of $v_o \sim (400 - 850) \text{ km s}^{-1}$ values lead to the range $\dot{M}_p \approx (3-5) \times 10^{10} \text{ g s}^{-1}$, depending upon the efficiency of the stellar wind to transport heat ($\Gamma \sim [1.01 - 1.13]$, upper and bottom panels of Table 2, respectively). The Ly α transit time variation obtained while increasing the coronal temperature varies from $\Delta t \sim 4.4 \text{ h}$ to $\Delta t \sim 5.5 \text{ h}$. Note from fig. 3 in VM03, that the observational Ly α transit time can be estimated as $> 4 \text{ h}$.

Finally, in Fig. 4 it is possible to see a comparison among the isotropic models, $\Gamma = 1.01$ (left-hand panel), and $\Gamma = 1.13$ (right-hand panel) of the maximum absorption value during transit as a function of the planetary mass-loss rate considering the line core limits C: [19-11] per cent. From the left-hand panel, we see that models with $\Gamma = 1.01$ emission slowly begin to reach saturation, whereas, as expected, signs of saturations are already met in the case with $\Gamma = 1.13$ and stellar wind temperature ($T_0 = 3 \text{ MK}$), resulting in the intersection of some of the lines. This is the reason why, unlike the general trend mentioned earlier, we find an increase of the absorption with increasing coronal temperature. That is, the bottom panel of Table 2 shows that, when varying T_0 from 3 to 5

MK with $\dot{M}_p = 5 \times 10^{10} \text{ g s}^{-1}$ the absorption values increase from 20.26 to 22.41.

It is worthwhile to notice that all these results are valid considering a fix value of \dot{M}_* . In order to test the influence of \dot{M}_* in the calculated Ly α planetary absorption we run two cases where \dot{M}_* is 0.1 and 10 of its fixed value ($\dot{M}_* = 9.0 \times 10^{-14} M_\odot \text{ yr}^{-1}$). The other model parameters are: $T_0 = 4 \text{ MK}$, $\Gamma = 1.13$ and $\dot{M}_p = 3 \times 10^{10} \text{ g s}^{-1}$. We found that the planetary absorption increases almost a 40% in the first case and diminishes by the same amount in the second case. This implies that the \dot{M}_p that better adjust the observational Ly α absorption values are $\dot{M}_p = 1 \times 10^{10}$ and $5 \times 10^{10} \text{ g s}^{-1}$, respectively.

4.2 Anisotropic planetary wind models

In Section 3 we introduced four anisotropic models inspired on the discussions in Adams (2011); García Muñoz (2007); Murray-Clay et al. (2009) and Yelle (2004). Table 3 shows the results obtained for the different planetary wind models ordered with decreasing absorption (see columns 2-4). From the results, we can see that the Day and Day-Night anisotropic models produce less absorption and a shorter transit time than the isotropic one. Plasma mostly evaporated from the illuminated side is rapidly ionized and thus absorption is less important than in the other escape models. The shortest transit time is produced when the planetary wind is emitted from the Day-Night model. The difference between this last model, with respect to the Day one, is because there is less material to be ionized given the lower initial planetary speed value (to allow the same \dot{M}_p). The largest absorptions and transit times occur for the Polar and Night models. As can be seen in figure 5, where a 3D view shows the density distribution for the absorbing material, the Day and Day-Night models exhibit smaller absorbing tails, and the longest belongs to the Polar model. This latter model exhibits greater neutral density (in comparison to the rest of the anisotropic models) available to absorb within the tail, and can propagate further before being heated and consequently ionized.

Fig. 6(a) shows the Ly α simulated normalized flux (to the out of transit value for the C limits) as a function of the wavelength for the same anisotropic models ($\dot{M} = 3 \times 10^{10} \text{ g s}^{-1}$ and $T = 4 \text{ MK}$), together with the corresponding isotropic model. Figs 6(b) and (c) show a zoom of the right- and left-hand wings of the absorption profile as a function of the wavelength for the previous mentioned cases. The evident blueshifted asymmetry in the line profiles is a consequence of the absorbing planetary material escaping towards the line-of-sight direction (VM03), being more pronounced in the Polar and Night cases, where the planetary mass-loss configuration favours the driving of absorbing material towards the line of sight.

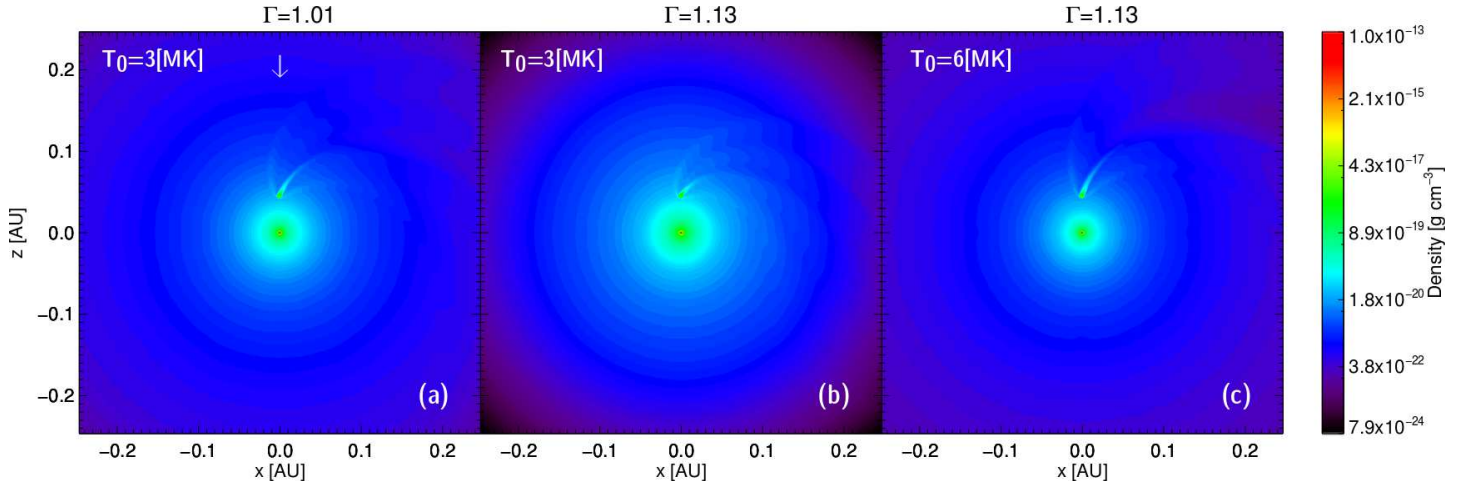


Figure 2. Orbital cuts of 3D HD simulation corresponding to the density stratification for a stellar wind temperature and polytropic index of (a) $T = 3$ MK, $\Gamma = 1.01$; (b) $T = 3$ MK, $\Gamma = 1.13$ and (c) $T = 6$ MK, $\Gamma = 1.13$. All figures are obtained when the planet is located at the same orbital position.

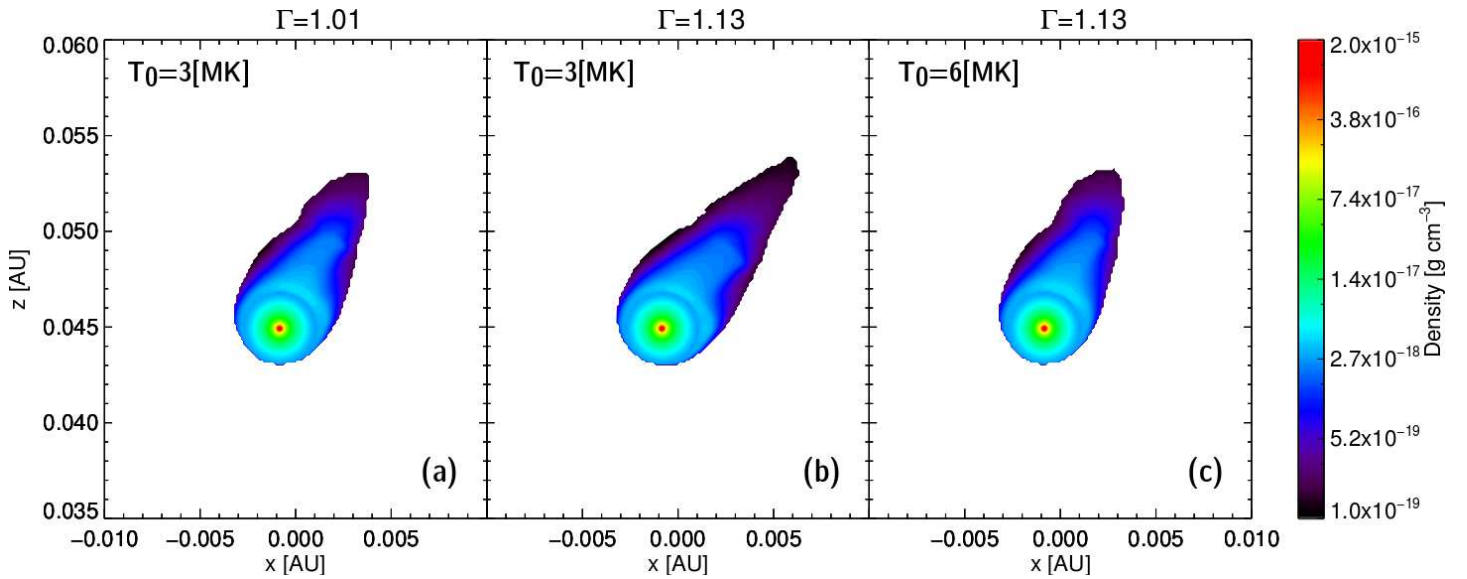


Figure 3. Enlarged orbital cuts of 3D HD simulation for $\dot{M}_p = 3 \times 10^{10} \text{ g s}^{-1}$ corresponding to a density stratification of the absorbing planetary material for a stellar wind temperature of (a) $T = 3$ MK, $\Gamma = 1.01$; (b) $T = 3$ MK, $\Gamma = 1.13$ and (c) $T = 6$ MK, $\Gamma = 1.13$. All figures are obtained when the planet is located at the same orbital position.

5 CONCLUSION

In this work, we have explored a wide range of parameters with the main purpose of studying the dynamic response of close-in exoplanets to different stellar wind conditions. The chosen system, HD 209458 is the most known among the many observed, and therefore has served as a good numerical laboratory. Initially, our aim was to find a mechanism that would help to determine the stellar wind velocity at the orbital position, yet not defined for the present system due to the need of better observational data. Nevertheless, from our results we have been able to narrow down some parameters. For a fixed \dot{M}_* , we found that the \dot{M}_p is not too sensitive to the stellar wind conditions, in comparison with the ranges reported in the literature. Observation of transits have found mass-loss rates in the range $10^9 - 10^{11} \text{ g s}^{-1}$ (see VM03; Lecavelier Des Etangs et al. 2010; Linsky et al. 2010 and Guo 2011). Assuming \dot{M}_p values varying in a reasonable range ($\dot{M}_p = [1-7] \times 10^{10} \text{ g s}^{-1}$) we could

constrain the planetary mass-loss rate by comparing the observational $\text{Ly}\alpha$ absorption with the numerically derived values. The range we found for \dot{M}_p is $\sim [3-5] \times 10^{10} \text{ g s}^{-1}$, where it changes a factor of ~ 1.7 for a change in temperature from $[3-7] \times 10^6 \text{ K}$, a variation of the stellar wind velocity in the range $\sim [250 - 850] \text{ km s}^{-1}$, and a polytropic index value between $\Gamma \sim [1.01 - 1.13]$. Also, our models give a variation of the transit time between $[4.4 - 5.5] \text{ h}$, which is in agreement with the minimum observed Δt (see fig. 3 by VM03 where we can estimate a $\Delta t > 4 \text{ h}$). A better observational determination of Δt could play an important role in solving part of the degeneracy in the inferred mass loss rate and stellar wind parameters. The $\text{Ly}\alpha$ planetary absorption depends on the \dot{M}_* value, thus assuming that a fix value of this parameter constraints the results. However, by studying a single model, we notice that while varying \dot{M}_* through a factor of 0.1 and 10 the \dot{M}_p that better adjusts

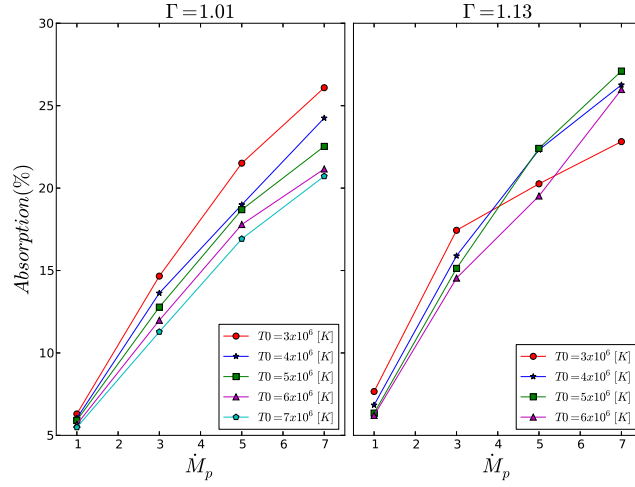


Figure 4. Maximum Ly α absorption during transit as a function of the planetary mass-loss rate for the isotropic models (considering the line core limits, C: [19-11] per cent) with different T_0 for $\Gamma = 1.01$ (left-hand panel) and $\Gamma = 1.13$ (right-hand panel).

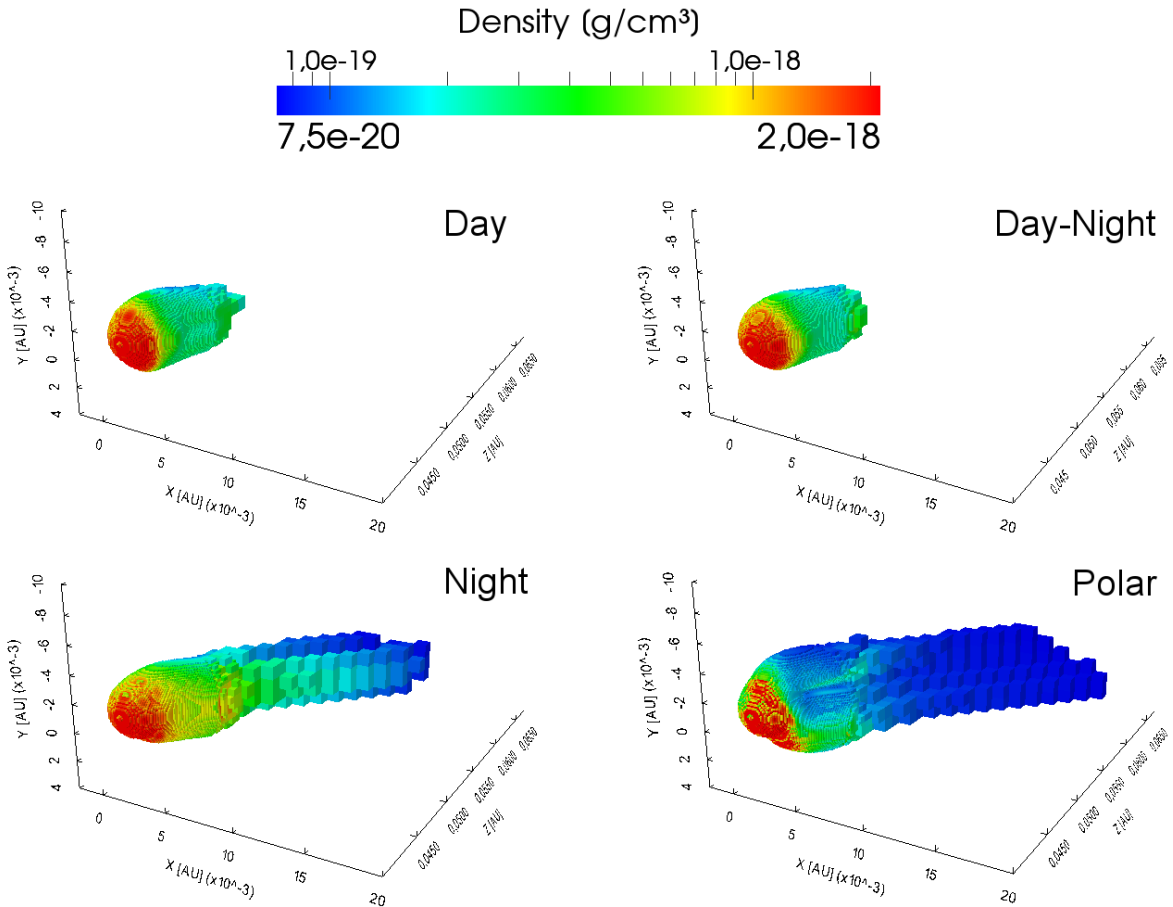


Figure 5. 3D surface density distribution of the absorbing material corresponding to the anisotropic planetary wind models, obtained for $\Gamma = 1.13$, $\dot{M}_p = 3 \times 10^{10} \text{ g s}^{-1}$ and stellar wind temperature of $T = 4 \text{ MK}$. Upper left: day; upper right: day-night; lower left: night and lower right: polar. All figures are obtained when the planet is located at the same orbital position.

T_0 (MK)	v_o (km/s)	$\dot{M}_p \times 10^{10}$ (g/s)	C: [19-11] per cent [-120, 100]km s ⁻¹	I: [11-6.8] per cent [-200, 200]km s ⁻¹	W: [7-3] per cent [-320, 200]km s ⁻¹	Δt (h)
3	429	1	6.30	2.76	2.01	4.4
		3	14.66	6.43	4.68	5.0 (a)
		5	21.51	9.72	7.05	5.5
		7	26.09	12.61	9.17	6.1
4	548	1	6.04	2.64	1.92	4.4
		3	13.63	5.97	4.34	5.0
		5	18.99	8.41	6.12	5.0
		7	24.25	11.72	8.53	5.5
5	657	1	5.91	2.59	1.88	4.4
		3	12.78	5.60	4.07	5.0
		5	18.69	8.23	5.99	5.0
		7	22.53	10.14	7.37	5.5
6	757	1	5.67	2.48	1.80	4.4
		3	11.98	5.25	3.82	4.4
		5	17.79	7.83	5.69	5.0
		7	21.16	9.47	6.89	5.0
7	852	1	5.49	2.40	1.75	4.4
		3	11.28	4.94	3.59	4.4
		5	16.92	7.42	5.39	4.4
		7	20.72	9.18	6.68	5.0
3	247	1	7.66	3.35	2.44	5.0
		3	17.44	7.67	5.58	5.0 (b)
		5	20.26	8.93	6.49	6.6
		7	22.82	10.10	7.35	7.2
4	388	1	6.84	2.99	2.18	4.4
		3	15.89	7.00	5.09	5.5
		5	22.32	10.07	7.32	6.1
		7	26.26	12.79	9.3	7.2
5	513	1	6.35	2.78	2.02	4.4
		3	15.13	6.64	4.83	5.0
		5	22.41	10.28	7.48	5.5
		7	27.10	13.99	10.17	6.7
6	630	1	6.21	2.72	1.98	4.4
		3	14.54	6.38	4.64	5.0 (c)
		5	19.52	8.69	6.32	5.0
		7	25.98	13.26	9.64	5.5

Table 2. Isotropic planetary wind models. Parameters and results for initial conditions with polytropic index upper: $\Gamma = 1.01$ and bottom: $\Gamma = 1.13$. Parameters: T_0 the coronal temperature, v_o is the stellar wind speed at the planet position and \dot{M}_p is the planetary mass-loss rate. Results: C the line core interval comparable with VM03 limits ([19-11] per cent); I the intermediate line range comparable with BJ07 limits ([11-6.8] per cent) and W the whole line interval comparable with VM04 limits ([7-3] per cent). Δt is the transit time. Results in boldface better adjust all the observational cases. Models noted as a, b and c (last column) correspond to Figs 2(a)-(c), respectively.

Model	C: [19-11] per cent	I: [11-6.8] per cent	W: [7-3] per cent	Δt [h]
Polar	28.40	14.11	10.26	5.6
Night	24.07	12.17	8.85	5.5
Isotropic	15.89	7.00	5.09	5.5
Day	15.53	6.85	4.98	5.1
Day-Night	12.76	5.59	4.07	5.0

Table 3. Absorptions and transit times for the anisotropic planetary atmospheric models with $\Gamma = 1.13$, $T_0 = 4$ MK, and $\dot{M}_p = 3 \times 10^{10}$ g s⁻¹. C, I, W and Δt are defined as in Table 2.

the observational Ly α absorption value changes in a factor of 0.3 and 1.7, respectively.

Another important result comes from studying the variation of the structure of the escaping atmosphere. Even though the present models are far from being realistic, they give us a hint on how to further study these type of systems. Still, we can conclude that there

is a noticeable effect produced by changes in the escaping atmosphere on the observed Ly α absorption. The Polar and Night side emitting models, show an enhanced absorption with respect to the isotropic and there is an appreciable reduction on the maximum absorption measured for the Day and Day-Night cases, where the Day-Night model shows the minor value. Note that for all isotropic

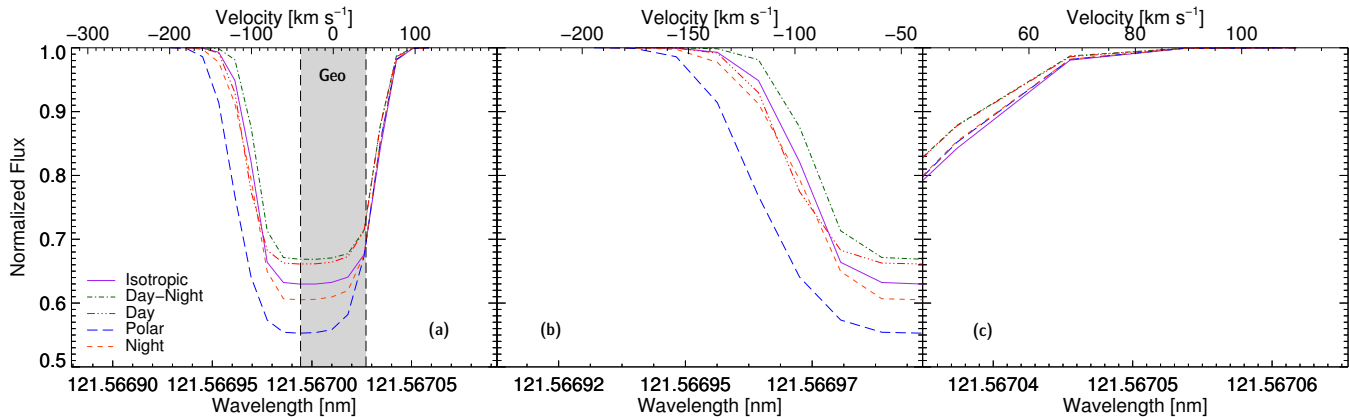


Figure 6. $\text{Ly}\alpha$ normalized flux (to the out of transit value and for the C range) as a function of the wavelength for the anisotropic models with $\dot{M} = 3 \times 10^{10} \text{ g s}^{-1}$ and $T = 4 \text{ MK}$, and the corresponding isotropic model. The grey stripe represents the excluded area due to geocoronal contamination: panel (a) shows a comparison among models with different planetary atmospheric structures as depicted in Fig. 1. Panels (b) and (c) show a zoom of the right- and left-hand wings for each case. All figures are obtained when the planet is located at the same orbital position.

and anisotropic models the velocity of the planetary escaping material ranges from $\sim [-160, 100] \text{ km s}^{-1}$, in accordance with the observational data.

More realistic models are necessary, specially if we want to venture on this last part. For instance, an improved model should include explicitly the photoionization of the planetary wind in the hydrodynamical calculation, even though, this is unlikely to produce an important effect on the $\text{Ly}\alpha$ absorption, because as the tail expands it becomes optically thin. Also, a similar study to the present one should be done with the inclusion of the systems magnetic fields, i.e. the almost certain planetary magnetic field and the stellar magnetic field is another.

PV, AR and AE acknowledge financial support from Conacyt grant 167611 and DGAPA-UNAM IN105312. Also, all authors acknowledge financial support from Conacyt-CONICET grant CAR 190489.

REFERENCES

- Adams F. C., 2011, *ApJ*, 730, 27
 Ben-Jaffel L., 2007, *ApJL*, 671, L61 (BJ07)
 Ben-Jaffel L., 2008, *ApJ*, 688, 1352 (BJ08)
 Ben-Jaffel L., Sona Hosseini S., 2010, *ApJ*, 709, 1284
 Charbonneau D., Brown T. M., Latham D. W., Mayor M., 2000, *ApJ*, 529, L45
 Ehrenreich D., Lecavelier Des Etangs A., Hébrard G., Désert J.-M., Vidal-Madjar A., McConnell J. C., Parkinson C. D., Ballester G. E., Ferlet R., 2008, *A&A*, 483, 933
 Ekenbäck A., Holmström M., Wurz P., Grieblmeier J.-M., Lammer H., Selsis F., Penz T., 2010, *ApJ*, 709, 670
 García Muñoz A., 2007, *Planet Space Sci.*, 55, 1426
 Guo J. H., 2011, *ApJ*, 733, 98
 Henry G. W., Marcy G. W., Butler R. P., Vogt S. S., 2000, *ApJ*, 529, L41
 Holmström M., Ekenbäck A., Selsis F. Penz T., Lammer H., Wurz P., 2008, *Nature*, 451, 970
 Koskinen T. T., Yelle R. V., Lavvas P., Lewis N. K., 2010, *ApJ*, 723, 116
 Lecavelier des Etangs A., Vidal-Madjar A., McConnell J. C., & Hébrard G., 2004, *A&A*, 418, L1
 Lecavelier Des Etangs A. et al., 2010, *A&A*, 514, A72
 Linsky J. L., Yang H., France K., Froning C. S., Green J. C., Stocke J. T., Osterman S. N., 2010, *ApJ*, 717, 1291
 Llama J., Wood K., Jardine M., Vidotto A. A., Helling Ch., Fossati L., Haswell C. A., 2011, *MNRAS*, 416, L41
 Murray-Clay R. A., Chiang E. I., Murray N., 2009, *ApJ*, 693, 23
 Osterbrock D. E. 1989, *Astrophysics of Gaseous Nebulae and Active Galactic Nuclei*, Mill Valley, CA, 422 pp.
 Preusse S., Kopp, A., Büchner J., Motschmann U., 2005, *A&A*, 434, 1191
 Raga A. C., Navarro-González R., Villagrán-Muniz, 2000, *Rev. Mex. de Astron. y Astrofís.*, 36, 67
 Rauer H., Roesler F., Scherb F., Schmidt H. U., Wegmann R., 1997, *A&A*, 325, 839
 Schneider J., Rauer H., Lasota J. P., Bonazzola S., Chassefiere E., 1998, *ASP Conf. Ser. Vol. 134, Brown Dwarfs and Extrasolar Planets*. Astron. Soc. Pac., San Francisco, p. 241
 Schneiter E. M., Velázquez P., Esquivel A., Raga M., Blanco-Cano X. 2007, *ApJ*, 671, L57 (SCH07)
 Tian F., Toon O. B., Pavlov A. A., De Sterck H., 2005, *ApJ*, 621, 1049
 Vidal-Madjar A., Lecavelier des Etangs A., Désert J.-M., Ballester G. E., Ferlet R., Hébrard G., Mayor M., 2003, *Nature*, 422, 143 (VM03)
 Vidal-Madjar A. et al., 2004, *APJL*, 604, L69 (VM04)
 Vidal-Madjar A., Lecavelier des Etangs A., Désert J.-M., Ballester G. E., Ferlet R., Hébrard G., Mayor M., 2008, *APJL*, 676, L57 (VM08)
 Vidal-Madjar, A. et al. 2011, *AAP*, 533, 4
 Vidotto A. A., Jardine M., Helling C., 2010, *ApJL*, 722, L168
 Vidotto A. A., Fares R., Jardine M., Donati J.-F., Opher M., Moutou C., Catala C., Gombosi T. I., 2012, *MNRAS*, 423, 3285
 Yelle R. V., 2004, *Icarus*, 170, 167
 Yelle R. V., 2006, *Icarus*, 183, 508